IEEE Photonics Journal
An IEEE Photonics Society Publication

Open Access

A Compact Fiber Optic Fabry–Perot Sensor for Simultaneous Measurement of Acoustic and Temperature

Volume 11, Number 6, December 2019

Xiaoying Liu
Junfeng Jiang
Shuang Wang
Kun Liu
Lei Xue
Xue Wang
Zhe Ma
Xuezhi Zhang
Yongning Zhang
Tiegen Liu

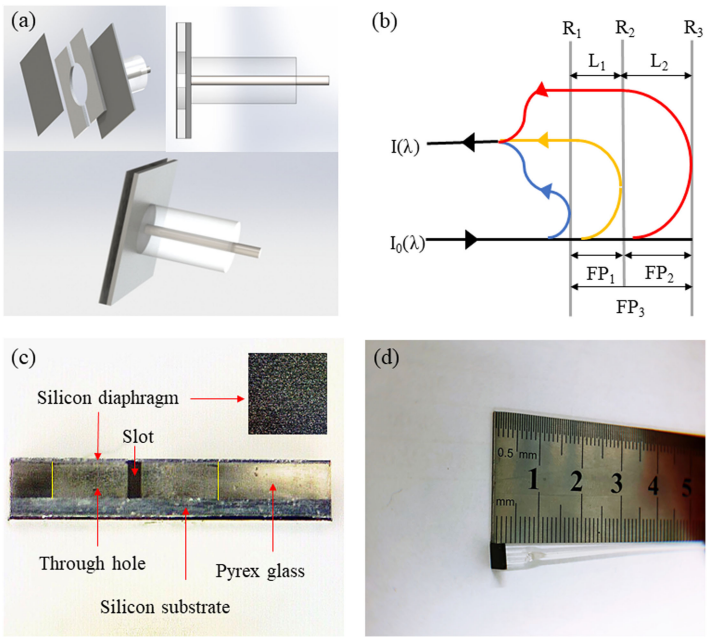

DOI: 10.1109/JPHOT.2019.2948045

A Compact Fiber Optic Fabry–Perot Sensor for Simultaneous Measurement of Acoustic and Temperature

Xiaoying Liu,[1,2] **Junfeng Jiang**,[1,2] **Shuang Wang**,[1,2] **Kun Liu**,[1,2] **Lei Xue**,[1,3] **Xue Wang**,[1,2] **Zhe Ma**,[1,2] **Xuezhi Zhang**,[1,2] **Yongning Zhang**,[1,2] **and Tiegen Liu** [1,2]

[1]School of Precision Instrument and Optoelectronics Engineering, Tianjin University, Tianjin 300072, China
[2]Key Laboratory of Optoelectronics Information Technology (Ministry of Education), Tianjin University, Tianjin 300072, China
[3]AVIC Chengdu CAIC Electronics Co., Ltd., Chengdu 610091, China

DOI:10.1109/JPHOT.2019.2948045

Manuscript received July 22, 2019; revised October 7, 2019; accepted October 15, 2019. Date of publication October 17, 2019; date of current version November 12, 2019. This work was supported in part by the National Natural Science Foundation of China under Grants 61735011, 61675152, and 61505139; in part by the Tianjin Natural Science Foundation under Grant 16JCQNJC02000; in part by the National Instrumentation Program of China under Grant 2013YQ030915; in part by the China Postdoctoral Science Foundation under Grant 2016M590200; and in part by the Open Project of Key Laboratory of Optoelectronics Information Technology under Grant 2019KFKT007. Corresponding authors: Junfeng Jiang and Shuang Wang (e-mail: jiangjfjxu@tju.edu.cn; shuangwang@tju.edu.cn).

Abstract: A compact fiber optic Fabry-Perot (F-P) sensor for simultaneous acoustic and temperature measurement has been proposed in the research. The sensor consists of silicon-glass-silicon sandwich structure by anodic bonding. The air F-P cavity with a circular hole and slots utilizes the deformation of the silicon membrane to realize acoustic measurement, and the silicon F-P cavity utilizes the temperature sensitivity of the refractive index of silicon to realize temperature measurement. The acoustic signal and temperature information could be recovered by acoustic and temperature demodulation method, respectively. The experimental results demonstrate that the sensor has a signal-to-noise ratio (SNR) of 53 dB and the acoustic sensitivity of 4.65 mV/Pa at 21 kHz, and the temperature sensitivity of 123.10 nm/°C at 20 °C∼120 °C. The proposed fiber optic F-P sensor has great potential for simultaneous acoustic and temperature measurement in aviation, due to its compact structure, mass production and immunity to electromagnetic interference.

Index Terms: Fiber optic sensor, Fabry-Perot sensor, acoustic, temperature.

1. Introduction

Measurements of acoustic characteristics and temperature are important in aviation industry, such as aeroengine in-duct sound filed and sound radiation from the nozzle for noise control optimization, temperature for health monitoring and combustion performance control [1]. The acoustic characteristics of aeroengine are high sound pressure level (SPL), and the maximum SPL of Boeing for the fuselage array application sensor can be as high as 172 dB [2]. In addition, both inlet pressure and temperature distortion will affect the aeroengine stability and its power output [3], thus the simultaneous measurement of the two parameters are useful. The present acoustic technology utilized in aeroacoustic fuselage is piezoresistive pressure transducer, which has disadvantage of

power consumption associated with biasing of piezoresistors, difficulty in expand array scale and vulnerable to electromagnetic interference. As an alternative, optical fiber sensing technology provides an ideal solution, due to its electronic-passive, multiplex capability and robustness in harsh environment.

Several kinds of fiber optic interferometer have been studied for acoustic detection. Pawar *et al.* [4] spliced a polarization-maintaining photonic crystal fiber (PM-PCF) between two single-mode fibers to form a Mach-Zehnder interferometer (MZI) to detect underwater acoustic signals. Li *et al.* [5] proposed a fiber-optic Michelson interferometer (MI) with a polypropylene/poly ethylene terephthalate (PP/PET) membrane to detect low frequency acoustic signal. Knudsen *et al.* [6] proposed a push-pull hydrophone based on the Sagnac interferometer (SI) to detect acoustic signal. Qi *et al.* [7] used phase-shifted fiber Bragg grating (FBG) as the sensor to detect ultrasonic waves by the encoded strain in the Bragg wavelength shift. Shao *et al.* [8] used a single mode fiber (SMF) and a micro suspended-core fiber to form a F-P cavity for acoustic measurement. Membrane-based F-P sensor has become more and more popular, because the elastic membrane is more sensitive to the vibration of the acoustic wave. Several types of elastic materials have been used as the pressure-sensitive membrane, such as polymer [9], [10], silver [11]–[13], silicon [14], [15] and graphene [16]–[18]. However, these sensors are mainly focused on the measurement of the acoustic signal. F-P sensors are also used for temperature measurement. Nakamura *et al.* [19] used a single polymer-cylinder-based F-P cavity for measurements of acoustic pressure and temperature. They attached a polymer cylinder with 100 μm length and gold film at the end of optical fiber to construct the sensor. Using a single F-P cavity makes it can only measure a parameter each time. Paul *et al.* [20] proposed a similar sensor structure. They put fibers on a mount and then deposited the polymer and gold film to construct a F-P cavity with 10.4 μm length. By improving the demodulation technique with laser wavelength dynamical tuning tracking the optimal bias point, they realized the simultaneous measurement of acoustic and temperature to some extent. The polymer material limits the maximum temperature measurement range to 70 °C. Yin *et al.* [21] used a hybrid F-P cavity constructed by silicon and glass materials to achieve static pressure and temperature measurement simultaneously.

In this paper, we propose a compact fiber optic F-P sensor for acoustic and temperature measurement simultaneously. The sensor head is formed by bonding silicon wafers of different thickness on both sides of the Pyrex glass with circular hole and slots, which constructs a serial connected F-P cavity. The air F-P cavity and the silicon F-P cavity are used for acoustic and temperature measurement, respectively. In terms of acoustic measurement, acoustic wave causes the deformation of the top silicon membrane to change the cavity length of the air F-P cavity, and the side slots allow air flow in and out freely. Meantime, the silicon F-P cavity, with high thermo-optic coefficient and thermal expansion coefficient of silicon, achieve temperature measurement. These results indicate that the sensor can recover acoustic signals and temperature information very well. The acoustic sensitivity is 4.65 mV/Pa at 21 kHz and the temperature sensitivity is 123.10 nm/°C at 20 °C ∼120 °C. The proposed sensor is mass producible, which is helpful of maintaining sensor performance consistency. High yields provide the potential for further cost-effective commercial development.

2. Principle

2.1 Sensor Fabrication

Fig. 1(a) presents the schematic diagram of the proposed compact fiber optic F-P sensor. The upper part is an exploded view of the structure and a two-dimensional structure, and the lower part is the assembled 3D structure. The sensor head consists of three layers connected in sequence, which are silicon membrane, Pyrex glass and silicon substrate. Pyrex glass is sandwiched between silicon membrane and silicon substrate. There is a center through hole and two side slots in Pyrex glass. The axial hole in the Pyrex glass constitutes an air cavity, and the slots make the air flow in and out the cavity freely. In Fig. 1(b), there exist three reflective surfaces, including: the front and

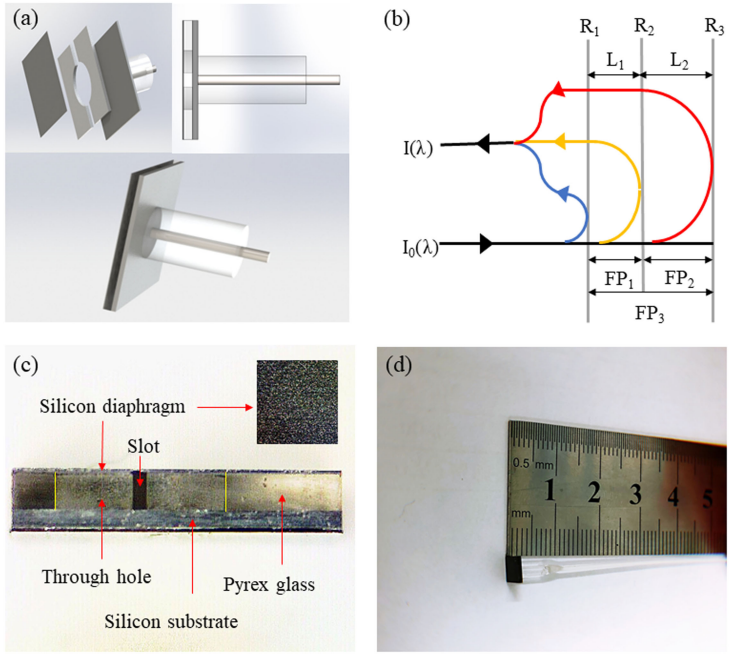

Fig. 1. (a) Schematic diagram of the sensor. (b) Interference mechanism of the sensor. (c) Microscope imaging of the sensor head. (d) Packaged F-P sensor.

the back reflective surfaces of the silicon substrate, and the inner reflective surface of the silicon membrane, which are marked as R_1, R_2, and R_3, respectively. The reflective surfaces R_1 and R_2 form FP_1, namely silicon cavity, and the cavity length is L_1. The reflective surfaces R_2 and R_3 form FP_2 and is called air cavity, with the cavity length of L_2. The reflective surfaces R_1 and R_3 form a long cavity FP_3 and the length of the cavity is $L_1 + L_2$.

The input beams reflected from the reflective surfaces R_1, R_2 and R_3 will interfere with each other. The total light intensity is [22]

$$I(\lambda) = I_1 + I_2 + I_3 - 2\sqrt{I_1 I_2}\cos(\phi_1) - 2\sqrt{I_2 I_3}\cos(\phi_2) + 2\sqrt{I_1 I_3}\cos(\phi_1 + \phi_2), \quad (1)$$

where I_1, I_2 and I_3 refer to the light intensities of the three reflected light, all of which are only slightly dependent on the incident wavelength λ, thus I_1, I_2 and I_3 could be considered to constant approximately. ϕ_1 and ϕ_2 denote respectively the propagation phase shifts of FP_1 and FP_2, and can be expressed as

$$\phi_1 = \frac{4\pi n_{si} L_1}{\lambda}, \phi_2 = \frac{4\pi n_{air} L_2}{\lambda}, \quad (2)$$

where n_{si} and n_{air} are the reflective index of silicon and air, respectively. According to Eq. (1), the reflection spectrum of the sensor is a linear superposition of three cosine functions, where different spectral frequency components correspond to different optical path differences (OPD) of the F-P cavity. The FP_1, FP_2, and FP_3 are corresponding to the fourth, the fifth, and the sixth term of Eq. (1), respectively. Therefore, the OPD of FP_1 and FP_2 can be independently obtained by extracting distinctive frequency component signal with appropriate bandpass filtering.

The sensor is fabricated as follows: First, a polished Pyrex glass wafer (BOROFLOAT 33) with a thickness of $\sim$500 μm is etched into structure unit array, each unit has a hole with a radius of $\sim$1250 μm and two slots with a width $\sim$200 μm. Next, a polished silicon wafer with the thickness of $\sim$315 μm is used as the silicon substrate and bonded to the abovementioned Pyrex glass wafer by anodic bonding. Similarly, the silicon membrane, a polished silicon wafer with the thickness of $\sim$50 μm, is attached to the other side of the Pyrex glass wafer. The outside surface of silicon

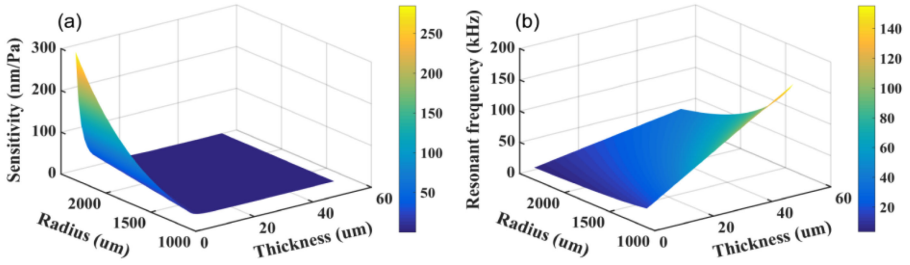

Fig. 2. (a) Theoretical acoustic pressure sensitivities of the sensor. (b) Theoretical resonant frequencies of the sensor.

membrane layer is roughened by a UV laser marking machine (EP-15-THG-S) to suppress its reflection and reduce the equivalent thickness of the membrane, as shown in the subgraph of Fig. 1(c). The bonded wafer is then sliced into hundreds of independent sensing heads with the size of 5 mm $\times$ 5 mm. Fig. 1(c) shows the side view microscopic image of the sensor head and we can see a thin silicon-Pyrex glass-thick silicon sandwich structure. Finally, the sensor head is connected to the SMF fixed by the glass ferrule with the UV glue to complete sensor packaging, as shown in Fig. 1(d).

2.2 Acoustic Sensing Principle

When the acoustic wave is loaded, the thin silicon membrane of the FP_2 is deformed. That is to say, the acoustic signal is finally converted into variation of the length of the FP_2 cavity. The deformation of the cavity length ΔL_2 will result in a change in the interference intensity $\Delta I(\lambda)$, which can be expressed as [23]

$$\Delta I(\lambda) = \left[\frac{8\pi n_{air}}{\lambda}\left(\sqrt{I_2 I_3}\sin(\phi_2) - \sqrt{I_1 I_3}\sin(\phi_1+\phi_2)\right)\right]\Delta L_2, \tag{3}$$

It can be seen that the change in the interference intensity $\Delta I(\lambda)$ is proportional to the change in the cavity length ΔL_2, from Eq. (3).

In the case of a small deformation (a deformation of less than 30% of the thickness of the membrane) is assumed, the elastic membrane and the externally applied pressure will have a fine linearity. The acoustic sensitivity of the sensor, the center deformation of the membrane under unit acoustic pressure, can be expressed as [24]

$$Y_C = \frac{3(1-\mu^2)R^4}{16Eh^3}, \tag{4}$$

where R and h are the membrane radius and thickness. E and μ are the Young's modulus and Poisson's ratio of the silicon, respectively. The resonant frequency of the membrane f_{00} is determined by [25]

$$f_{00} = \frac{\alpha_{00}}{4\pi}\left[\frac{E}{3\omega(1-\mu^2)}\right]^{1/2}\left(\frac{h}{R^2}\right), \tag{5}$$

where α_{00} is a constant related to the vibration modes, and it is 10.21 for the lowest natural frequency. ω is the mass density of the membrane.

For silicon material, $E = 190$ GPa, $\mu = 0.278$, $\omega = 2.33\,\mathrm{g/cm^3}$. Figs. 2(a) and (b) show the dependence of sensor acoustic pressure sensitivity, resonant frequency on hole radius and membrane thickness, respectively.

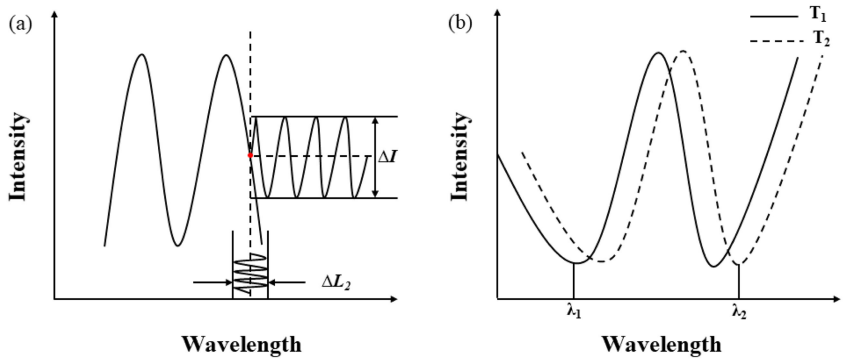

Fig. 3. (a) Demodulation principle of acoustic pressure. (b) Demodulation principle of temperature.

2.3 Temperature Sensing Principle

The original OPD of FP_1 is $\Delta_1 = 2n_{si}L_1$, when subjected to a change in temperature, the OPD of FP_1 will change, which can be expressed as

$$\Delta_1 = 2\left(n_{si} + \frac{\partial n}{\partial T}\Delta t\right)(1 + \alpha_{si}\Delta t)L_1, \tag{6}$$

where $\frac{\partial n}{\partial T}$ is thermo-optic coefficient of silicon, α_{si} is thermal expansion coefficient of silicon, and Δt is temperature change. When we adopt the following parameters: $\frac{\partial n}{\partial T} = 1.86 \times 10^{-4}K^{-1}$,$\alpha_{si} = 2.6 \times 10^{-6}K^{-1}$, and $n_{si} = 3.47$ [26], [27]. In theory, the calculated temperature sensitivity of FP_1 is 122.86 nm/°C. According to Eq. (6), the temperature measurement can be achieved by recovering the OPD of FP_1 through analyzing the extracted frequency component signal.

2.4 Demodulation Method

To obtain the reflection spectra of the FP_1 and FP_2 cavities, respectively, we use FFT and wavelength tracking methods to demodulate the hybrid interference spectra. First, the cubic spline interpolation algorithm is used to obtain the equally spaced frequency samples $\delta\nu$, then the FFT is used to convert the wavelength of the reflection spectra into the frequency domain. Afterwards, we use two appropriate bandpass filters to search for the interference spectra corresponding to the frequency components of FP_1 and FP_2, respectively. It can also track the wavelength shift of the two interference spectra separately. In order to avoid the phase ambiguity problem, firstly, we obtain a rough OPD of each F-P cavity, which is $\Delta = 2k/(N\delta\nu)$, where N represents the number of sampling points of FFT, k represents the abscissa of the peak corresponding to the frequency component. Then, we could select a certain peak wavelength λ_m and calculate its interference order m, which is $m = \Delta/\lambda_m$. Accurate OPD of each F-P cavity can be calculated by the obtained interference order and peak wavelength. By using the proposed method, the tracking wavelength is always at the same interference order. The method achieves high accuracy, wide range measurements.

Figs. 3(a) and (b) reflect the demodulation method of acoustic pressure and temperature, respectively. For acoustic measurement, the wavelength of the laser is fixed at a slope of one linear side of the interference spectra, and the sensor has a higher sensitivity where slope of the wavelength is bigger. The independent interference spectra corresponding to FP_1 is filtered out for temperature sensing. From Eq. (6), as the temperature increases, the OPD of FP_1 increases and the wavelength shifts to the right at the same interference order.

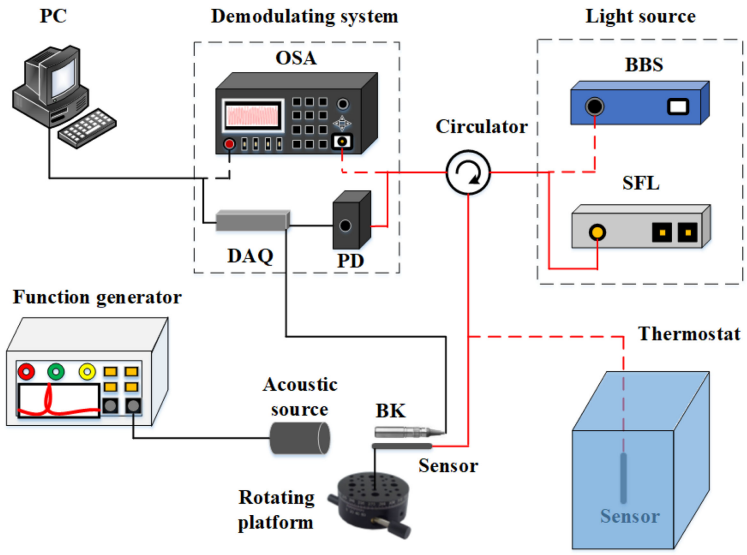

Fig. 4. Schematic diagram of the sensing system configuration.

3. Experiment Results

Fig. 4 shows the schematic diagram of the fiber optic sensing experiment system. For acoustic measurement, a light wave is emitted by a single frequency laser (SFL) with output power of 6 mW into the circulator to the sensor. The reflected light coming back from the sensor passes through the circulator again and is transmitted into a photodetector (PD) and converted into the electric signal, which is shown on the PC via the data acquisition (DAQ) to process further. The acoustic source is driven by a function generator to generate sine waves. A standard microphone (B & K) is placed side by side with the sensor to calibrate the acoustic source signal. The sensor is fixed on a manual rotating platform, directly opposite the acoustic source and the distance is fixed as 4 cm. For temperature measurement, the sensor is placed in a thermostat with an accuracy of 0.001 °C. A light wave is emitted by a broadband source (BBS) with output power of 10 mW into the circulator to the sensor. The reflected light coming back from the sensor passes through the circulator again and is received by an optical spectrum analyzer (OSA), then the data is processed further by PC. We can use the wavelength division multiplexer (WDM) and the demultiplexing multiplexer to simplify the experimental system and realize simultaneous acoustic and temperature measurement. A tunable laser and a distributed feedback laser that have different wavelength ranges can be combined by a two-channel WDM. The signal light reflected from the sensor is split into two beams of the signal light with different wavelength ranges by a demultiplexing multiplexer, and transmitted to two PDs at the same time. The received two channel output signals can then be processed separately with the two demodulation methods, which allow the two parameters measurement simultaneously.

The reflection spectra of the compact optical fiber F-P sensor is shown in Fig. 5(a). Fig. 5(b) shows the result of the FFT transformation, we can see there are three main frequency components peak 1, 2, and 3. According to the demodulation method, we can calculate the OPDs corresponding to the three peaks, and the values are 1000 μm, 2186.1 μm and 3186.1 μm, respectively. Using the structure parameters of the sensor, the theoretical OPDs of FP_1, FP_2 and FP_3 are as follows:

$$\begin{cases} \Delta_1 = 2n_{si}L_1 = 2 \times 3.47 \times 315 = 2186.1\,\mu\text{m} \\ \Delta_2 = 2n_{air}L_2 = 2 \times 1 \times 500 = 1000\,\mu\text{m} \\ \Delta_3 = \Delta_1 + \Delta_2 = 3186.1\,\mu\text{m} \end{cases} \tag{7}$$

We can see that the demodulated OPDs agree with the theoretical values well from Eq. (7). Therefore, the peak 1, 2, and 3 correspond to the cavity of FP_2, FP_1 and FP_3, respectively.

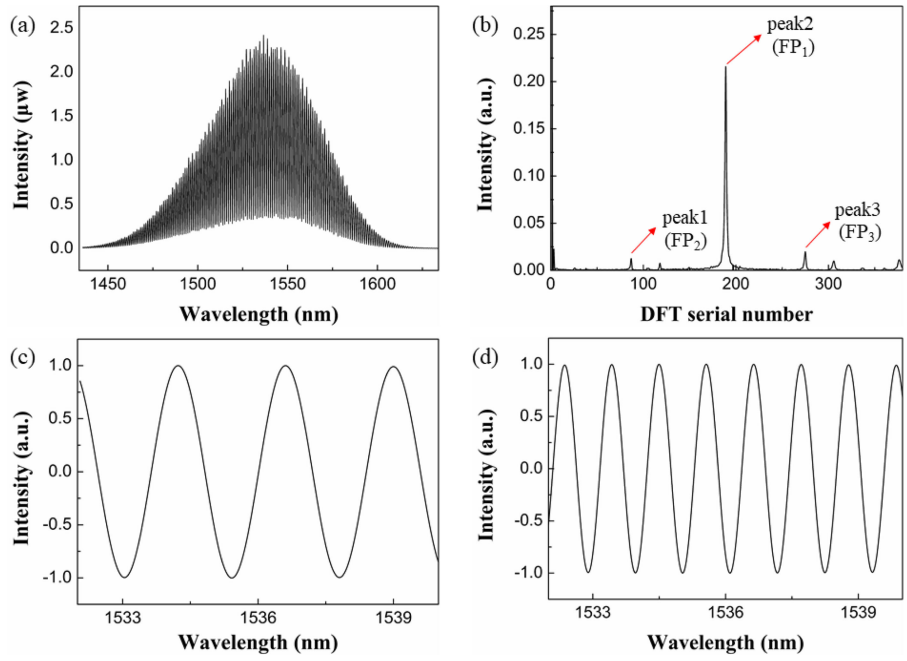

Fig. 5. (a) Reflection spectra of the sensor. (b) Spatial frequency spectra of the reflection light. (c) Independent interference spectra of FP_2 after filter. (d) Independent interference spectra of FP_1 after filter.

The other small peaks are caused by multiple beam interference, they can be filtered out and have no impact on our experiment. Figs. 5(c) and (d) correspond to the independent interference spectra of the filtered FP_2 and FP_1, respectively.

The output peak-to-peak voltage of the function generator is 10 V, corresponding to the acoustic pressure ~180 Pa (SPL 139 dB). The responses of the sensor to 15 kHz and 21 kHz sinusoidal single frequency acoustic signal are presented in Fig. 6. It is seen from Fig. 6(a) that the time-domain output signal of the sensor is sine waveform with a peak-to-peak voltage of 630 mV. Its frequency spectrum is shown in Fig. 6(b), we can see that the frequency is 15 kHz, which is agree with the frequency of the acoustic source, and the sensor has a SNR of 53 dB. The results of ultrasonic signal of 21 kHz are shown in Figs. 6(d) and 6(e). Fig. 6(d) shows the time-domain output signal of the sensor is sine waveform with a peak-to-peak voltage of 807 mV. Its frequency spectrum is shown in Fig. 6(e), we can see that the frequency is 21 kHz, which is agree with the frequency of the acoustic source, and the sensor has a SNR of 70 dB. Fig. 6(c) and 6(f) are the frequency spectrum with the BK responding to 15 kHz sinusoidal single and 21 kHz ultrasonic single, respectively. We can see from Fig. 6(b) and 6(d) that there are some other beatings like peaks except the highest peak we need, too. Compared with the results of the BK and considering our sensor is less sensitive, we think they may be caused by the acoustic source and electronic circuit noise.

The driving frequency of function generator is then fixed at 21 kHz and its driving voltage increases from 1 V to 10 V (corresponding to the acoustic pressure from 20 Pa to 180 Pa) with a step 1 V. Fig. 7(a) shows that the peak-to-peak voltage of the time-domain response of the sensor increases linearly. The sensitivity of sensor is 4.65 mV/Pa at 21 kHz, which is equivalent to the membrane deformation sensitivity of 1.40 nm/Pa. According to Eq. (4), it can be calculated that the equivalent thickness of the thin silicon membrane of FP_2 cavity after processed by the UV laser marking machine is 11.65 μm. Thus, the resonant frequency of the sensor f_{00} is calculated as 33 kHz according to Eq. (5).

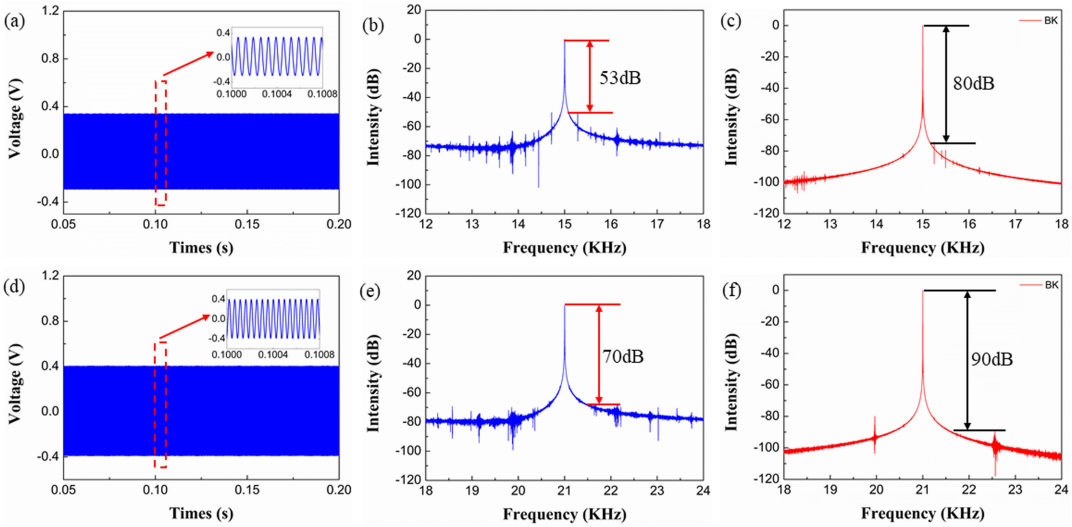

Fig. 6. (a) The time-domain output signal with the sensor responding to 15 kHz sinusoidal single. (b) The frequency spectrum with the sensor responding to 15 kHz sinusoidal single. (c) The frequency spectrum with the BK responding to 15 kHz sinusoidal single. (d) The time-domain output signal with the sensor responding to 21 kHz sinusoidal single. (e) The frequency spectrum with the sensor responding to 21 kHz sinusoidal single. (f) The frequency spectrum with the BK responding to 21 kHz sinusoidal single.

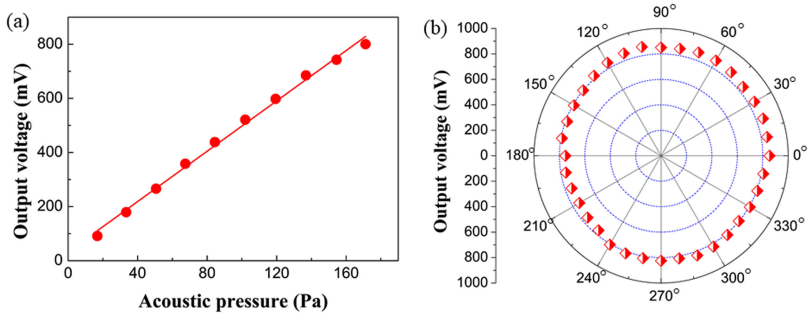

Fig. 7. (a) Output voltage versus acoustic pressure at 21 kHz. (b) The direction response of the sensor.

We fix the sensor on a manual rotating platform, and the sensor head of the sensor is at the center of the rotating platform. The acoustic source is then placed 4 cm from the sensor, and the driving frequency of the function generator is fixed at 21 kHz and its driving voltage is fixed at 10 V. We keep the acoustic source direction unchanged and rotate the sensor from 0° to 360° with a step 10° to test its directivity. The direction response experimental result is shown in the Fig. 7(b) with a polar plot expression, and each point represents the output voltage at a certain angle. The values of radius scale division from small to large are 200 mV, 400 mV, 600 mV, 800 mV and 1000 mV, respectively. From Fig. 7(b), we can see that the output voltage of the sensor is around 800 mV at different angles, which shows that the sensor has good omnidirectional characteristics.

Fig. 8 shows the temperature measurement experiment result. The sensor undergoes a process of heating and cooling, from 20 °C to 120 °C, with an interval of 10 °C. As the temperature increases, the peak of the interference pattern gradually shifts to a longer wavelength, as shown in Fig. 8(a), which is consistent with the theoretical analysis of temperature measurement. The relationship between temperature and the OPD of FP_1 is shown in Fig. 8(b). The OPD of FP_1 has an excellent linearity with the temperature ($R^2 = 0.9998$). The measured temperature sensitivity is 123.10 nm/°C

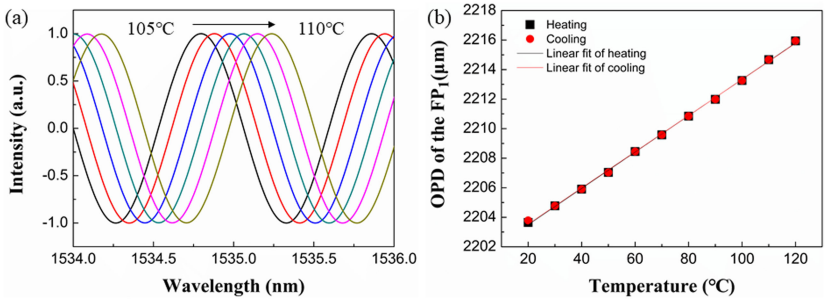

Fig. 8. (a) Interference spectra shift of FP_1 when the temperature varies from 105 to 110 °C. (b) Dependence of the silicon cavity on temperature.

and is close to the theoretical value 122.86 nm/°C. The response curve during heating and cooling stage almost coincide, which indicates the sensor has a fine repeatability.

4. Conclusions

We have proposed and demonstrated a compact fiber optic F-P sensor for acoustic and temperature simultaneous measurement. The principle of measurement is analyzed theoretically. The proposed omnidirectional sensor has a SNR of 53 dB, 4.65 mV/Pa of the acoustic sensitivity at 21 kHz and 123.10 nm/°C of the temperature sensitivity at 20 °C ∼120 °C. The sensor consisted of a silicon-glass-silicon sandwich structure provides the possibility of mass production, and is expected to be used for acoustic and temperature measurement of aeroengine. Furthermore, the performance of the sensor could be further improved by optimizing the size and thickness of silicon membrane.

References

[1] I. Mohammed, A. R. A. Talib, M. T. H. Sultan, and S. Saadon, "Temperature and heat flux measurement techniques for aeroengine fire test: A review," in *Proc. 6th Innov. Aerosp. Eng. Technol. Conf.*, Kuala Lumpur, Malaysia, 2016, vol. 152, p. 012036.
[2] M. D. Williams, B. A. Griffin, T. N. Reagan, J. R. Underbrink, and M. Sheplak, "An AIN MEMS piezoelectric microphone for aeroacoustic applications," *J. Microelectromech. Syst.*, vol. 21, pp. 270–283, 2012.
[3] W. M. Braithwaite and R. H. Soeder, "Combined pressure and temperature distortion effects on internal flow of a turbofan engine," *J. Aircr.*, vol. 17, pp. 468–472, 1979.
[4] D. Pawar, C. N. Rao, R. K. Choubey, and S. N. Kale, "Mach-Zehnder interferometric photonic crystal fiber for low acoustic frequency detections," *Appl. Phys. Lett.*, vol. 108, 2016, Art. no. 041912.
[5] L. Liu *et al.*, "Fiber-optic Michelson interferometric acoustic sensor based on a PP/PET diaphragm," *IEEE Sensors J.*, vol. 16, no. 9, pp. 3054–3058, May 2016.
[6] S. Knudsen and K. Blotekjaer, "An ultrasonic fiber-optic hydrophone incorporating a push-pull transducer in a Sagnac interferometer," *J. Lightw. Technol.*, vol. 12, no. 9, pp. 1696–1700, Sep. 1994.
[7] W. Qi and O. Yoji, "High-sensitivity ultrasonic phase-shifted fiber Bragg grating balanced sensing system," *Opt. Exp.*, vol. 20, pp. 28353–28362, 2012.
[8] Z. Shao, Q. Rong, F. Chen, and X. Qiao, "High-spatial-resolution ultrasonic sensor using a micro suspended-core fiber," *Opt. Exp.*, vol. 26, pp. 10820–10832, 2018.
[9] J. Jiang *et al.*, "Non-contact ultrasonic detection in low-pressure carbon dioxide medium using high sensitivity fiber-optic Fabry-Perot sensor system," *J. Lightw. Technol.*, vol. 35, no. 23, pp. 5079–5085, Dec. 2017.
[10] L. Chen, C. Chan, W. Yuan, S. K. Goh, and J. Sun, "High performance chitosan diaphragm-based fiber-optic acoustic sensor," *Sensors Actuators A, Phys.*, vol. 163, pp. 42–47, 2010.
[11] X. Feng, S. Jinhui, G. Kui, L. Hefei, H. Rongqing, and Y. Benli, "Fiber-optic acoustic pressure sensor based on large-area nanolayer silver diaphragm," *Opt. Lett.*, vol. 39, pp. 2838–2840, 2014.
[12] F. Guo, T. Fink, M. Han, L. Koester, J. Turner, and J. Huang, "High-sensitivity, high-frequency extrinsic Fabry-Perot interferometric fiber-tip sensor based on a thin silver diaphragm," *Opt. Lett.*, vol. 37, pp. 1505–1507, 2012.
[13] B. Liu, J. Lin, J. Wang, C. Ye, and P. Jin, "MEMS-based high-sensitivity Fabry–Perot acoustic sensor with a 45° angled fiber," *IEEE Photon. Technol. Lett.*, vol. 28, no. 5, pp. 581–584, Mar. 2016.
[14] F. Wang, Z. Shao, J. Xie, Z. Hu, L. Hong, and Y. Hu, "Extrinsic Fabry–Pérot underwater acoustic sensor based on micromachined center-embossed diaphragm," *J. Lightw. Technol.*, vol. 32, no. 23, pp. 4628–4636, Dec. 2014.

[15] R. Kressmann, M. Klaiber, and G. Hess, "Silicon condenser microphones with corrugated silicon oxide/nitride electret membranes," *Sensors Actuators A, Phys.*, vol. 100, pp. 301–309, 2002.
[16] J. Ma, H. Xuan, H. L. Ho, W. Jin, Y. Yang, and S. Fan, "Fiber-optic Fabry–Pérot acoustic sensor with multilayer graphene diaphragm," *IEEE Photon. Technol. Lett.*, vol. 25, no. 10, pp. 932–935, May 2013.
[17] Y. Wu *et al.*, "A highly sensitive fiber-optic microphone based on graphene oxide membrane," *J. Lightw. Technol.*, vol. 35, no. 19, pp. 4344–4349, Oct. 2017.
[18] W. Ni *et al.*, "Ultrathin graphene diaphragm-based extrinsic Fabry-Perot interferometer for ultra-wideband fiber optic acoustic sensing," *Opt. Exp.*, vol. 26, pp. 20758–20767, 2018.
[19] K. Nakamura and K. Nimura, "Measurements of ultrasonic field and temperature by a fiber optic microprobe," *Acoust. Sci. Technol.*, vol. 21, pp. 267–269, 2000.
[20] M. Paul, H. Andrew, S. Adam, Z. Edward, and B. Paul, "A Fabry-Pérot fiber-optic ultrasonic hydrophone for the simultaneous measurement of temperature and acoustic pressure," *J. Acoust. Soc. Amer.*, vol. 125, pp. 3611–3622, 2009.
[21] J. Yin *et al.*, "Batch-producible fiber-optic Fabry–Pérot sensor for simultaneous pressure and temperature sensing," *IEEE Photon. Technol. Lett.*, vol. 26, no. 20, pp. 2070–2073, Oct. 2014.
[22] X. Wang *et al.*, "High-accuracy hybrid fiber-optic Fabry-Pérot sensor based on MEMS for simultaneous gas refractive-index and temperature sensing," *Opt. Exp.*, vol. 27, pp. 4204–4215, 2019.
[23] D. Ming, T. Chang-Ping, Z. Tao, R. Yun-Jiang, X. Lai-Cai, and H. Meng, "Refractive index measurement using photonic crystal fiber-based Fabry-Perot interferometer," *Appl. Opt.*, vol. 49, pp. 1593–1598, 2010.
[24] C. Fu, W. Si, H. Li, D. Li, P. Yuan, and Y. Yu, "A novel high-performance beam-supported membrane structure with enhanced design flexibility for partial discharge detection," *Sensors*, vol. 17, 2017, Art. no. E593.
[25] X. Zou, W. Nan, T. Ye, C. Niezrecki, J. Chen, and X. Wang, "Rapid miniature fiber optic pressure sensors for blast wave measurements," *Opt. Lasers Eng.*, vol. 51, pp. 134–139, 2013.
[26] H. Li, "Refractive index of silicon and germanium and its wavelength and temperature derivatives," *J. Phys. Chem. Reference Data*, vol. 9, pp. 561–658, 1980.
[27] G. Cocorullo and I. Rendina, "Thermo-optical modulation at 1.5 μm in silicon etalon," *Electron. Lett.*, vol. 28, pp. 83–85, 1992.